AIAA JOURNAL
Vol. 35, No. 12, December 1997

Computational Investigation of Shock-Enhanced Mixing and Combustion

Sang-Hyeon Lee,* In-Seuck Jeung,† and Youngbin Yoon‡
Seoul National University, Seoul 151-742, Republic of Korea

A computational investigation of shock-enhanced mixing and combustion is presented. To understand the influences of the mixing process on the combustion process, the mixing characteristics of the reacting case are compared with those of the nonreacting case. Parametric studies varying the conditions of fuel injection are conducted to find the trends of the mixing and combustion processes. Three-dimensional Navier–Stokes equations with a chemical reaction model and k–ω turbulence model are used. The upwind method of Roe's flux difference splitting scheme is adopted. It is shown that the mixing process has a strong influence on the combustion process, whereas the combustion process does not have any significant effect on the mixing process. The combustion process is divided into two mixing regimes: a convection-dominated regime, where the burning rate increases with distance from the injection plane, and a diffusion-dominated regime as one moves downstream, where burning rate is constant. In the parametric studies, varying the fuel pressure with the fuel density held fixed makes little difference, whereas varying the fuel density makes a significant difference in mixing rate and burning rate. A prediction of minimum combustor length for complete combustion is made.

Nomenclature

$\boldsymbol{E}, \boldsymbol{F}, \boldsymbol{G}$	= flux vectors in physical coordinate system
$\boldsymbol{E}_v, \boldsymbol{F}_v, \boldsymbol{G}_v$	= diffusive vectors in physical coordinate system
h_i	= height of injector nozzle plane
M	= Mach number
$\dot{m}$	= mass flow rate
Pe, s	= Peclet number for mass diffusion
p	= static pressure
$\boldsymbol{Q}$	= solution vector
q	= heat flux
Re	= Reynolds number
T	= temperature
u, v, w	= velocity components
x, y, z	= Cartesian coordinates
Y	= mass fraction
z_j	= jet liftoff height, hydrogen mass flux center normalized by h_i
Γ	= circulation normalized by $u_\infty h_i$
ρ	= density
ω	= vorticity vector

Subscripts

i	= injector
j	= injected hydrogen
r	= reaction step
s	= species index
x, y, z	= partial derivative to x, y, z coordinate, respectively
0	= stagnation
∞	= inlet condition

Introduction

THE design of the combustor of a supersonic combustion ramjet (scramjet) engine requires very efficient fuel–air mixing because of the short residence time of the air within the engine. The residence time of air in hypersonic airplane engines is only on the order of 1 ms for typical flight conditions. Within this short period of time, the air must be mixed with the fuel and then burned without excessive aerodynamic drag to achieve maximum thrust. The concept of shock-induced vorticity has been introduced as one of the possible mechanisms to enhance the fuel–air mixing in scramjet combustors.[1–3] It has been reported that the generation of streamwise vorticity is an efficient way of enhancing fuel–air mixing in hypersonic flows. The streamwise vorticity induces a large-scale convection that causes the air to roll up from the bottom edge of the fuel stream and be more rapidly mixed with the fuel. One of the simplest methods for generating streamwise vorticity is by shock-induced baroclinic torque. The generation mechanism of baroclinic torque can be explained by the baroclinic source term in the simplified vorticity equation

$$\rho \frac{\mathrm{D}}{\mathrm{D}t}\left(\frac{\boldsymbol{\omega}}{\rho}\right) = \frac{1}{\rho^2}\nabla\rho \times \nabla p$$

If the pressure gradient is not parallel to the density gradient in a fluid element, vorticity is generated. In shock-enhanced mixing, the dynamics of the vorticity is controlled by the incident shock strength and the density gradient between fuel and air.

The concept of shock-enhanced mixing was suggested by studies of the transmission and reflection of a weak shock wave from cylindrical and spherical gas inhomogeneities, investigated experimentally by Rudinger and Somers[4] and later by Haas and Sturtevant.[5] Marble et al.[6] first proposed shock-enhanced mixing in nonuniform gas streams for its potential application to scramjet combustors. Jacobs[7] verified mixing enhancement in this problem by experimentally studying the passage of a weak shock wave through a cylindrical helium region embedded in air. Distortion of the helium interface into a vortex pair structure was observed. In terms of numerical simulations, the Hass and Sturtevant[5] experiment has been simulated by Picone and Boris.[8] Also, Yang et al.[9] computed the two-dimensional analogy of the shock-induced mixing problem without chemical reactions. Drummond[10] simulated the full three-dimensional, steady shock-induced mixing problem with reaction. Ton et al.[11] studied numerically the two-dimensional analogy of the three-dimensional shock-enhanced mixing model and showed that the shock-enhanced mixing is not strongly influenced by combustion and subsequent heat release.

Marble et al.[12] conceived a geometry model of an injector system in which the basic concept of shock-generated streamwise vorticity could be incorporated into a scramjet combustor. Marble's model (Fig. 1) consists of alternate compression ramps and expansion troughs with the injecting nozzle placed at the end of each ramp.

Received Sept. 24, 1996; revision received July 25, 1997; accepted for publication July 29, 1997.

*Graduate Research Assistant, Department of Aerospace Engineering. Student Member AIAA.

†Professor, Department of Aerospace Engineering. Senior Member AIAA.

‡Instructor, Department of Aerospace Engineering. Member AIAA.

Table 1 Hydrogen-oxidation chemical kinetics[a]

No.	Reaction	Forward			Backward		
		A	N	E	A	N	E
1	$H + O_2 \leftrightarrow OH + O$	2.2E+14	0.0	8,455	1.5E+13	0.0	0
2	$O + H_2 \leftrightarrow OH + H$	7.5E+13	0.0	5,586	3.0E+13	0.0	4,429
3	$H_2 + OH \leftrightarrow H + H_2O$	2.0E+13	0.0	2,600	8.4E+13	0.0	10,116
4	$2OH \leftrightarrow O + H_2O$	5.3E+12	0.0	503	5.8E+13	0.0	9,059
5	$H_2 + M \leftrightarrow 2H + M$	5.5E+18	−1.0	51,987	1.8E+18	−1.0	0
6	$H_2O + M \leftrightarrow OH + H + M$	5.2E+21	−1.5	59,386	4.4E+20	−1.5	0
7	$OH + M \leftrightarrow O + H + M$	8.5E+18	−1.0	50,830	7.1E+18	−1.0	0
8	$O_2 + M \leftrightarrow 2O + M$	7.2E+18	−1.0	59,340	4.0E+17	−1.0	0

[a] $k_r = AT^N \exp(-E/RT)$ in $cm^3 mole^{-1} s^{-1}$ or $cm^6 mole^{-2} s^{-1}$ and E in cal $mole^{-1}$.

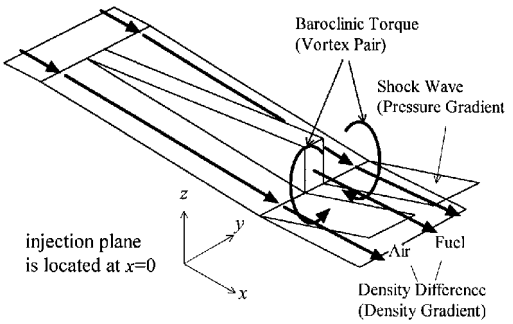

Fig. 1 Schematics of shock-enhanced mixing in Marble's model.

As the flow through the trough is turned parallel to the freestream, an oblique shock is formed, through which the pressure gradient is produced. At the same time, a density gradient perpendicular to the pressure gradient is produced by the density difference between the injectant and air. Thus, a baroclinic torque is produced. As a result of vorticity shed from the injector ramp and baroclinic torque, two vortices of opposite directions, called a vortex pair, are produced downstream of each injector. The vortex pair accelerates the fuel–air mixing without excessive aerodynamic drag and helps the fuel penetrate into the airstream. This method also exploits the injection of fuel as thrust. Waitz et al.[13,14] studied the mixing process (without reaction) by experimental and numerical methods and found that the shock-enhanced mixing in Marble's model of an injector system is a feasible way of enhancing fuel–air mixing in a hypervelocity flow condition. Lee et al.[15] studied the geometry effects on shock-enhanced mixing and showed that shock intersection has an adverse effect on shock-enhanced mixing. However, there are not enough numerical investigations including chemical reactions for Marble's model. The present study is an investigation of the combustion characteristics of shock-enhanced mixing.

The primary objective is to analyze the influence of the mixing process on the combustion process when the shock-enhanced mixing is incorporated into Marble's model. The combustion process utilizing shock-enhanced mixing is basically controlled by the mixing process. Hence, the combustion characteristics can be analyzed by the concept of mixing regime classified according to the dominant mixing mode: flow convection and mass diffusion. One of the two modes will play a dominant role in each region of fuel–air mixing. At the near field of the fuel nozzle, the convections due to baroclinic torque and shock waves have strong influences on fuel–air mixing; therefore, the near field may be considered to be the convection-dominated regime. On the other hand, at the far field, the flow convection gradually loses its influence on the fuel–air mixing as the flow acceleration mechanisms disappear and stable, enclosed streamlines around the fuel are formed by the vortex pair. In this region, the diffusion mode has more influence and, finally, plays a dominant role in fuel–air mixing. Therefore, the far field may be considered to be the diffusion-dominated regime. Hence, the analysis of the combustion region may be carried out using the concept of regions where different types of mixing are dominant.

Parametric studies varying the conditions of fuel injection were conducted to find the trends of the mixing and combustion processes, while the conditions of the airflow are held fixed at those described by Marble.[16] Two ways of varying the fuel injection conditions were considered: 1) fuel pressure varied with fuel density held fixed and 2) fuel density varied with fuel pressure held fixed. The fuel temperature is changed by the variation of fuel density or pressure according to the equation of state. The effects of pressure and density gradients between the fuel and air on the combustion were systematically investigated. To investigate the mixing characteristics, parameters such as circulation in the y–z plane, penetration distance, mixing rate, and burning rate were studied.

The concept of mixing regime and the parametric studies result in information about the design parameters for the scramjet combustor. In a mixing-controlled combustion process, it takes a long time to burn the fuel, which requires a long combustor for complete combustion. It is necessary to determine the parameters that set the combustor length. The estimation of the combustor length is difficult because of excessive computing time requirements. Hence, one objective of this study is to determine the parameters that set the combustor length so as to suggest a method for predicting the combustor length.

Method of Calculations

Governing Equations

The three-dimensional Navier–Stokes equations with chemical reactions are expressed in the following form[17–19]:

$$\frac{\partial \boldsymbol{Q}}{\partial t} + \frac{\partial \boldsymbol{E}}{\partial x} + \frac{\partial \boldsymbol{F}}{\partial y} + \frac{\partial \boldsymbol{G}}{\partial z} = \frac{\partial \boldsymbol{E}_v}{\partial x} + \frac{\partial \boldsymbol{F}_v}{\partial y} + \frac{\partial \boldsymbol{G}_v}{\partial z} + \boldsymbol{W}$$

The formulas and data of viscosity, thermal conductivity, and binary diffusivity are taken from Ref. 20. The intermolecular potential function is Lennard–Jones 12–6 potential. The viscosity of a pure gas is obtained from the Chapman–Enskog equation, and the viscosity of a gas mixture is calculated with the Wilke method. The thermal conductivity of a pure gas is obtained from the Eucken method, and the thermal conductivity of gas mixture is calculated with the Wassiljewa equation modified by Mason and Saxena. The diffusivity of a binary gas mixture is obtained from the Chapman–Enskog equation, and the diffusivity of a gas mixture is calculated with Blanc's law. The data of constant pressure specific heat are taken from the NASA polynomial[21] that covers up to 5000 K.

The vector $\boldsymbol{W}$ is the source term for chemical reaction. The production rate of sth species is expressed in the following form:

$$\dot{\rho}_s = M_s \sum_r (v''_{s,r} - v'_{s,r}) \left[k_{fr} \prod_s \left(\frac{\rho_s}{M_s} \right)^{v''_{s,r}} - k_{br} \prod_s \left(\frac{\rho_s}{M_s} \right)^{v'_{s,r}} \right]$$

where v'_s and v''_s are the forward and backward reaction coefficients respectively. An eight-step, seven-species reaction model is used. The reaction rates of all of the reaction steps are expressed in Arrhenius form, and the Arrhenius coefficients are obtained from the data of Refs. 22 and 23 and are shown in Table 1.

In this work, the k–ω turbulence model equations[24,25] are used to calculate turbulent viscosity. In these equations, a model for the dilatation–dissipation term ($\overline{\rho u'_{i,i} u'_i}$) suggested by Wilcox[24] is included to predict the compressibility effects. The turbulent diffusivity and turbulent conductivity are obtained from turbulent viscosity. The turbulent Prandtl number and turbulent Schmidt number are both set to 0.9 (Refs. 24 and 26).

A finite volume method is used to discretize the three-dimensional, thin-layer Navier–Stokes equations and turbulence model equations. To obtain the flux vector with an upwind method at the surface of the grid cell, Roe's flux difference splitting scheme[27] is used. The MUSCL scheme[28] is used to obtain a higher order of accuracy in spatial discretization. The lower–upper symmetric Gauss–Seidel scheme[29] is used for the time integration of nonreacting case, and the lower–upper symmetric successive overrelaxation scheme[30] is used for the time integration of the reacting case.

Calculation Grid and Flow Conditions

The geometry and grid system near the injector are shown in Fig. 2. The geometry of the injector system is the same as that of Waitz et al.[13,14] Three cross sections are located at the inlet, the injection plane, and downstream, respectively. To obtain a fine solution near the walls, grid points are clustered near the walls. The number of grid points of the primary grid system is $210 \times 40 \times 65$ (=546,000). To check grid independence, three grid systems with different numbers of grid points are used; the numbers of grid points are $190 \times 24 \times 48$ (=218,880, about 40% of primary grid system) for the second grid system, $210 \times 32 \times 57$ (=383,040, about 70% of primary grid system) for the third grid system, and $230 \times 48 \times 72$ (=794,880, about 146% of primary grid system) for the fourth grid system.

The flow conditions of the inlet air shown in Table 2 are taken from Ref. 16 and are the conditions for a hypersonic airplane flying at 31.5 km at a speed of Mach 18. The fuel used in this investigation is hydrogen, which is generally taken for the fuel of a hypersonic airplane engine. The flow conditions of hydrogen are shown in Table 3. Case A is a reference for comparison with the other cases (Fig. 3). The fuel temperature is 1000 K, and the fuel pressure is 1 atm. Two sets of parametric studies are performed by varying the conditions of fuel injection. In the first set of cases, A, B1, and B2, the fuel pressure is varied while the fuel densities (and flow rates) are fixed. This allows one to study the pressure effect on mixing and combustion. The fuel pressures for cases B1 and B2 are one-half and one-quarter, respectively, that for case A. The temperature of the fuel changes with the variation of pressure according to the equation of state. In the second set of cases, A, C1, and C2, the fuel density is varied while the fuel pressure is held fixed. This allows one to study the effect of density gradient, i.e., baroclinic torque, between the fuel and air on the mixing; the fuel densities for cases C1 and C2 are twice and four times, respectively, that for case A. Also, the temperatures change with the variation of density. Consequently, case C2 has the lowest density difference between the fuel and air. The change of the fuel temperature results in a change of the Mach number of the fuel.

Table 2 Flow conditions of air

p_∞, atm	1.0
T_∞, K	1500
ρ_∞, kg/m^3	0.2337
u_∞, m/s	4492
M	6.0

Table 3 Flow conditions of hydrogen

	Case A	Case B1	Case B1*[a]	Case B2	Case B2*	Case C1	Case C2
p/p_∞	1.0	0.50	1.0	0.25	1.0	1.0	1.0
T/T_∞	$\frac{2}{3}$	$\frac{1}{3}$	0.406	$\frac{1}{6}$	0.248	$\frac{1}{3}$	$\frac{1}{6}$
ρ/ρ_∞	0.105	0.105	0.172	0.105	0.283	0.21	0.42
u/u_∞	1.0	1.0	0.919	1.0	0.908	1.0	1.0
M	1.88	2.65	2.205	3.73	2.78	2.65	3.73

[a]Asterisk denotes the properties compressed insentropically to p_∞.

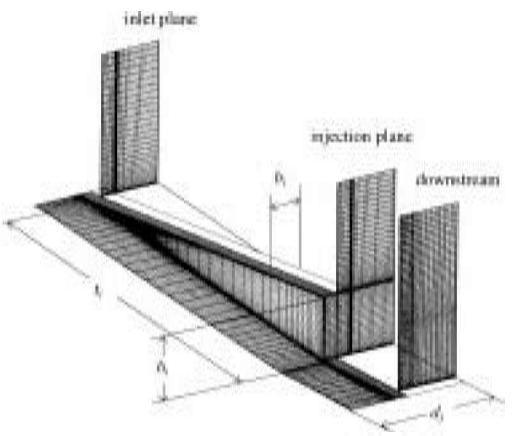

Fig. 2 Geometry and grid system near injection plane: injector height h_i = 1.0, trough length t_i = 6.0, injector width b_i = 0.5, and distance between injectors d_j = 2.0, all in inch scale.

For cases A, C1, and C2, the nozzle exit pressure is equal to the freestream pressure. Hence, one does not expect much expansion or compression of the jet downstream of the nozzle exit. However, this is not the case for conditions B1 and B2. For these two cases, the jet will be considerably compressed downstream of the nozzle because the nozzle exit pressures are only 0.5 and 0.25 times the freestream pressure, respectively. The values of cases B1* and B2* show the conditions reached by isentropically compressing the jet to the freestream pressure.

Results

Code Validation and Grid Independence

The solutions of the governing equations converge on the values with little unsteadiness. After the number of iterations exceeds 5000, the L2 norm of the pressure difference due to time marching in the whole domain is below the order of 10^{-5} and there are no realizable changes of circulation, penetration distance, mixing rate, and burning rate. Hence, the solutions are taken as steady. The computational code used in this investigation gives good agreement with the experimental results of Waitz et al.[14] The k–ω turbulence model predicts precisely the mixing rate experimental data, whereas the calculation without the turbulence model can not predict the mixing rate trends.[15] To check grid independence, calculations on the three different grid systems are conducted, and the results are shown in Fig. 4. Even though the calculation on the second grid system is made where the number of grid points is about 40% of primary grid system, it shows trends similar to those of the primary grid system with slightly underestimated circulation, penetration distance, and mixing rate. The results on the third and fourth grid systems show almost the same results as those on the primary grid system.

Influences of Mixing on the Combustion Process

To grasp the general trend of the combustion process, global views of the flowfield are plotted. Figure 3 shows the combustion process of case A. The number under each cross section is the distance from the injection plane normalized by injector height. Figure 3a shows the fuel distribution and pressure contours. The left-hand side of each cross section shows the fuel mass-fraction contours and the right-hand side shows the pressure contours. Two shock waves, one induced by the injector wedge and the other induced at the end of expansion trough, propagate upward. The shape of the fuel pattern can be explained by the vortex pair and the relative position of the shock waves. At the near field of the injection plane, air is entrained underneath the fuel due to the vortex pair, and the pressure over the fuel is raised because of the recompression of the expansion wave over the fuel region. Hence, the air pushes the fuel upward, and the high-pressure region over the fuel blocks the upward motion of fuel, which elongates the shape of the fuel jet in the lateral direction. After the fuel jet passes away from the shock waves, its shape is determined by the vortex pair. The fuel jet is divided into two halves and penetrates into the airstream with only small changes of the shape. The mass fraction contours of the OH radical and H_2O are plotted in Fig. 3b. The left-hand side of a cross section represents OH mass-fraction contours, whereas the right-hand side represents H_2O mass-fraction contours. Figure 3b shows that autoignition occurs at the mixing zone and that the flame propagates along the vortex pair and finally engulfs the fuel divided into two parts. The OH and H_2O near the stagnation point (on the bottom wall) come from

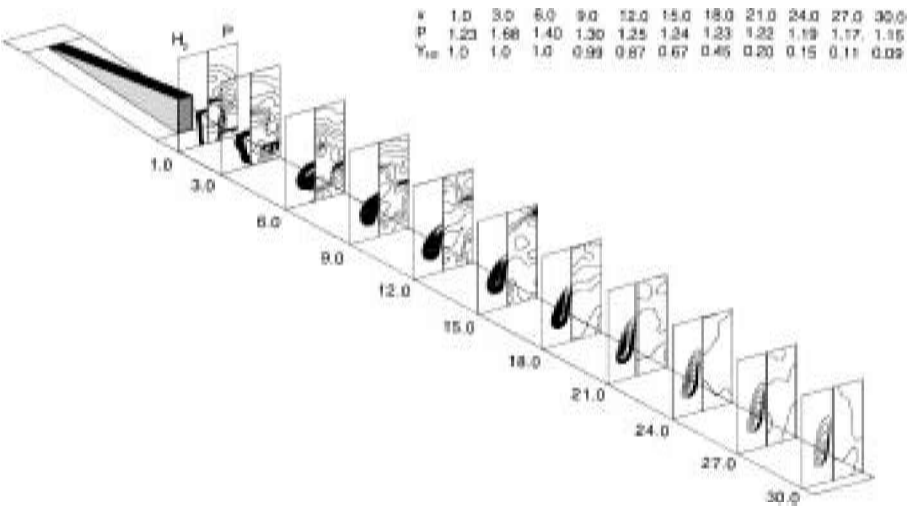

a) Mass-fraction contours of H_2 (left) and pressure contours (right)

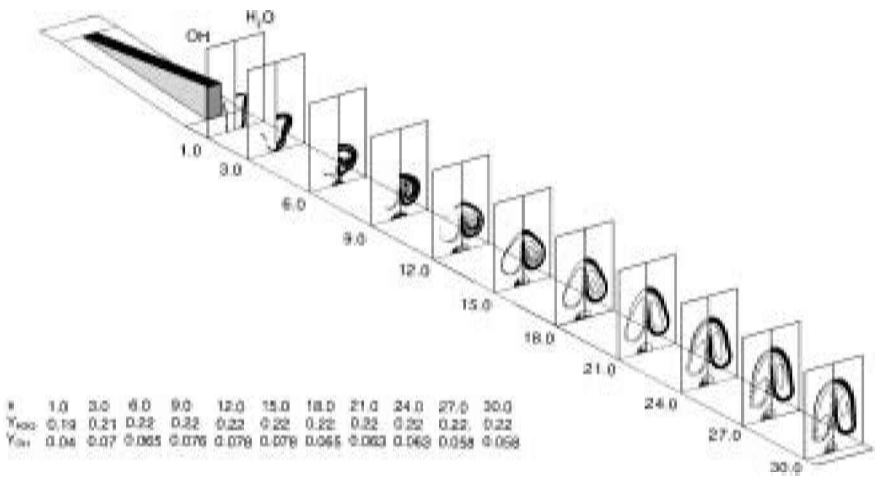

b) Mass-fraction contours of OH (left) and H_2O (right)

Fig. 3 Global view of mixing and combustion process (case A, $T_j = 1000$ K, $p_j = 1$ atm). Tabulated numbers denote the maximum values of parameters at each cross section.

the combustion of the fuel captured in the counter-rotating vortices located underneath the main vortices.

To measure the influences of the mixing process on combustion characteristics, the reacting and nonreacting cases are compared. Figure 4 shows the comparisons of circulation (Fig. 4a), penetration distance (Fig. 4b), and mixing rate (decay rate of maximum fuel mass fraction) (Fig. 4c). The circulation and baroclinic source term are defined in the following forms:

$$\Gamma = \frac{h_i}{u_\infty} \iint_{y,z} \left(\frac{\partial v}{\partial z} - \frac{\partial w}{\partial y} \right) \mathrm{d}y\, \mathrm{d}z$$

and

$$\text{baroclinic source} = \frac{1}{\rho_\infty p_\infty} \iint_{y,z} |\nabla \rho \times \nabla p|\, \mathrm{d}y\, \mathrm{d}z$$

The change of circulation is affected by the change of baroclinic source. The increase of circulation arises after the increase of baroclinic source, and the decrease of circulation arises after the decrease of baroclinic source. There are time delays between the changes of baroclinic source and the changes of circulation.

There is little difference between reacting and nonreacting cases in circulation, penetration distance, and mixing rate. This is believed to be because chemical reaction, i.e., heat release, has little influence on the generation of vorticity in a supersonic flowfield, whereas the mixing process is strongly influenced by the vorticity field.[11] Hence, the mixing process in shock-enhanced mixing strongly affects the combustion process, whereas the combustion process hardly affects the mixing process. These results indicate that the combustion process could be decoupled from the mixing process with only minor differences in the trend of mixing-controlled combustion.

Classification of Mixing Regime

In general, there are two dominant mechanisms in the fuel–air mixing process: flow convection and mass diffusion. Each mechanism plays a dominant role in different conditions. To check the dominance of the two mixing modes, two factors are considered: the history of the Peclet number and the formation of the enclosed stable streamlines. The Peclet number denotes the convection velocity vs the diffusivity. Hence, higher Peclet number means that the mixing capability of convection is higher than that of mass diffusion. The histories of the Peclet number are plotted in Fig. 5. The Peclet number is defined in the following form:

$$Pe, s = \iint_{y,z} \rho_{H_2} \frac{u\sqrt{v^2 + w^2}\, h_i}{D_{H_2}}\, \mathrm{d}y\, \mathrm{d}z \Bigg/ \iint_{y,z} \rho_{H_2} u\, \mathrm{d}y\, \mathrm{d}z$$

The axial component (x direction) of velocity is not considered in the convection velocity because it does not contribute to the mixing process. The Peclet number is averaged with hydrogen mass flux. Hence, a high Peclet number indicates that the flow convection is dominant in the fuel–air mixing process. As shown in Fig. 5, two distinct regions are classified with respect to Peclet number. The near field of the injection plane, where x is smaller than 10, represents large changes of Peclet numbers, and the far field, where x is larger than 10, shows almost constant values of Peclet number. At the near field of the injection plane, a sharp increase of Peclet number occurs due to the flow acceleration mechanism, such

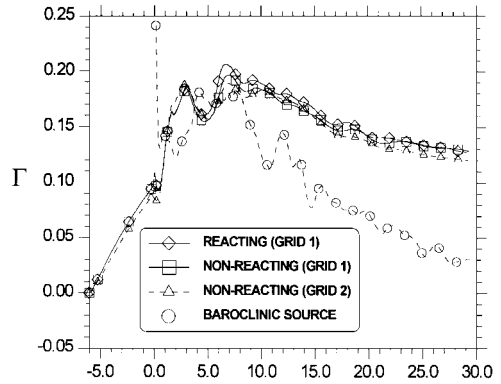

a) Circulation normalized by inlet air velocity and injector height (u_∞ , h_i)

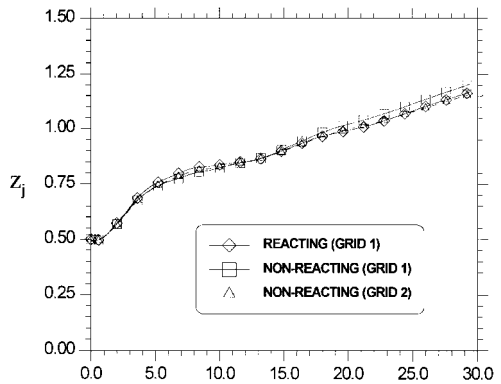

b) Penetration distance normalized by injector height h_i

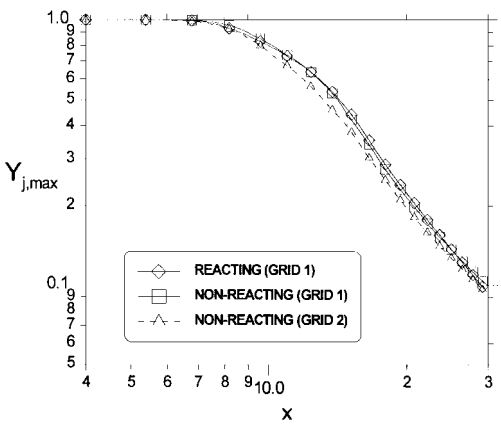

c) Mixing rate expressed by decay rate of maximum mass fraction

Fig. 4 Comparison between reacting and nonreacting cases.

as baroclinic torque, and the pressure gradient made by the shock wave. The sharp decreases after the peak are due to the flow deceleration by the high-pressure region over the fuel and to the increase of the mass diffusivity. At the far field, all of the cases show almost the same value of Peclet number, which is low and almost constant. This suggests that there are no significant flow acceleration mechanism. Another factor that should be considered is the formation of stable streamlines in y–z plane. If stable enclosed streamlines around the fuel are formed, the physical variables are almost uniform along the enclosed streamline and the mass diffusion normal to the streamlines plays a dominant role in the mixing process. Figures 3a and 4a show that the vortex pair keeps almost the same shape and the circulation maintains almost the same value at the far field of the injection plane, which suggests that mass diffusion plays a dominant role in fuel–air mixing at the far field.

From these facts, it can be said that there are two distinct regions where the dominant mechanism of the mixing is different. The near field of the fuel injection plane has a convection-dominated mixing regime due to the flow acceleration mechanism. The far field of the fuel injection plane has a diffusion-dominated mixing regime due

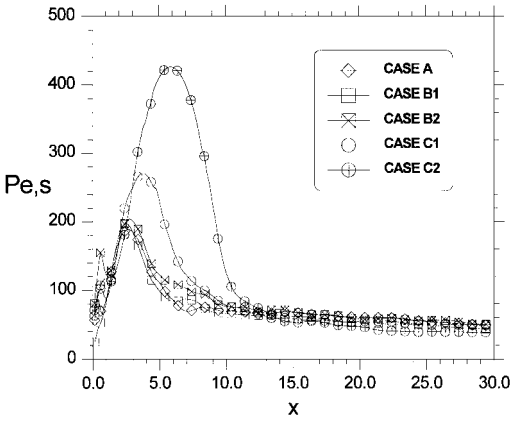

Fig. 5 Histories of Peclet number averaged with hydrogen mass flux.

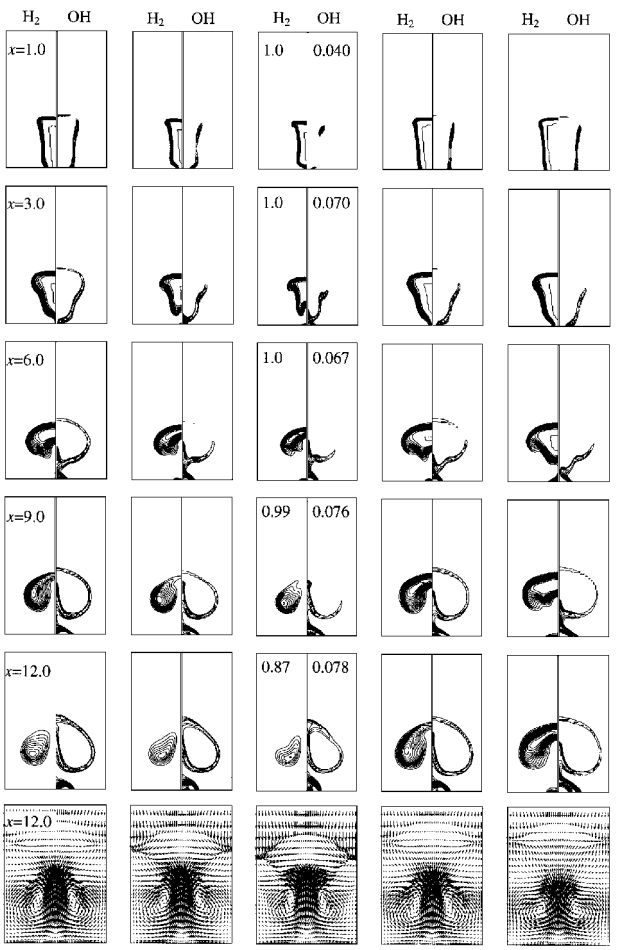

Case A Case B1 Case B2 Case C1 Case C2

Fig. 6 Combustion processes at near field; numbers of central columns are the maximum mass fractions of H_2 and OH, respectively; the last row shows velocity vector fields. Maximum speed in y–z plane is $0.2u_\infty$.

to the disappearance of the significant flow acceleration mechanism and the formation of stable enclosed streamlines.

Parametric Studies

Figure 6 shows the combustion processes of all of the cases at the near field of the injection plane. Even though the temperature of the injected hydrogen is quite low (250 K in the cases of B2 and C2), a self-ignited combustion occurs due to the high air temperature of 1500 K. In all cases the ignition occurs from the edge of fuel contours and the flame front rolls up to the vortex pair. The velocity vector fields at the bottom of Fig. 6 show that two counter-rotating vortex flows (vortex pair) are formed, and the flame regions are captured by the vortex pair in every case. Intense combustion occurs in the

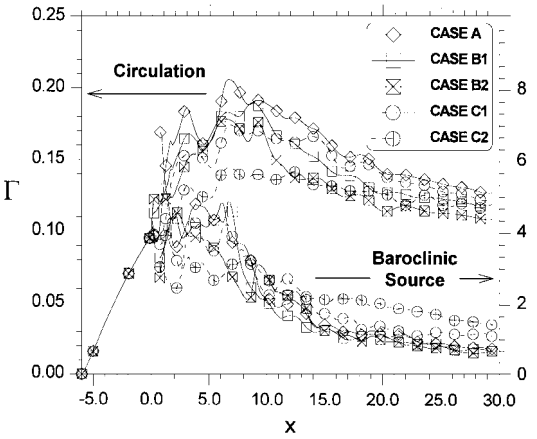

Fig. 7 Comparison of circulation normalized by inlet air velocity and injector height (u_∞, h_i) and baroclinic source normalized by inlet density and pressure (p_∞, ρ_∞).

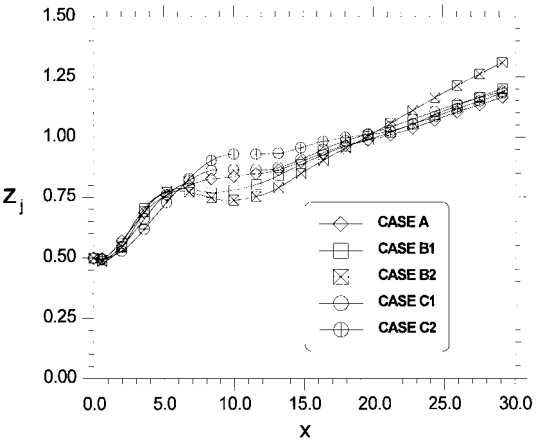

Fig. 8 Comparison of penetration distance normalized by injector height h_i.

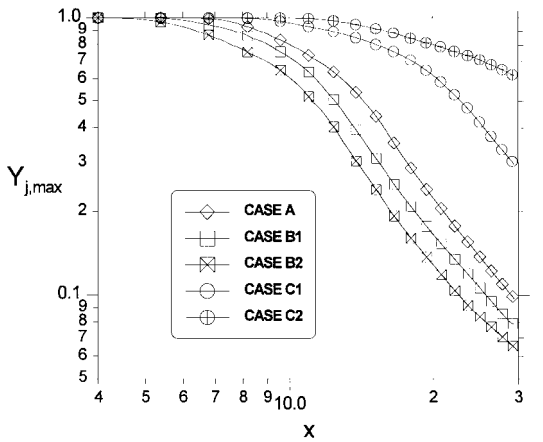

Fig. 9 Comparison of mixing rate expressed by decay rate of maximum hydrogen mass fraction plotted on log-log scale.

lower region of the fuel, where the high-temperature inflow of air due to the shock-induced vorticity causes intense fuel–air mixing. The shape of the flame is influenced by pressure and density of the fuel. Cases B1 and B2 have smaller flames than case A because those cases with lower pressure than that of the airstream have to be compressed up to the air-stream. Cases C1 and C2 have larger flames than case A because those cases with higher density than case A are less compressed than case A.

Figure 7 shows the comparison of the circulations in y–z plane normalized by the injector height and the velocity of inlet air. The circulation trend is similar to that of Waitz et al.[14] The increase of circulation before the injection plane (where $x < 0$), which is a large portion of streamwise circulation, is generated by the ramp. The increase of circulation after the injection plane is due to baroclinic torque. The decrease after the peak is due to the high-pressure region over the fuel region caused by the recompression of the expansion wave (see Fig. 3a). Among cases A, C1, and C2, case A with the highest density gradient (lowest density ratio ρ_j/ρ_∞) shows the highest circulation at the near field due to the highest intensity of baroclinic source. Case C2 shows the slowest decay of circulation at the far field due to the highest intensity of baroclinic source. This is because case C2 has the slowest mixing rate and there remains a density difference between fuel and air at the far field. Although cases A, B1, and B2 have the same density ratio (ρ_j/ρ_∞), they have different circulation trends because of different fuel pressures. Cases B1 and B2 with lower pressure than that of the airstream have to be compressed up to the airstream. When the fuel jets for cases B1 and B2 are compressed isentropically up to the freestream pressure level, their normalized densities would be 0.172 and 0.283 instead of 0.105 (see Table 3). Hence, the baroclinic torque would be less for cases B1 and B2 than for case A, and the circulations would also be expected to be less for cases B1 and B2 than case A.

Figure 8 shows the comparison of penetration distance, the distance of the mass center of fuel from the wall. The trend of the penetration is similar to the computational result of Waitz et al.[13,14] At the near field (convection-dominated regime), fuel penetration is achieved only by the penetration of the lower part of the fuel because the upper part is blocked by the high-pressure region over the fuel. The high-pressure region over the fuel stream decelerates the upward flow of the fuel, which results in the reduction of the slope of penetration distance and the high-pressure region under the fuel. After the fuel passes away from the injection plane, the fuel again starts to penetrate into the airstream due to the high pressure under the fuel. At the far field (diffusion-dominated regime), the fuel penetrates with a constant slope because there is no flow acceleration mechanism after the fuel passes away from the shock waves. The different histories of penetration distances among all of the cases can be explained with the flow acceleration mechanism and the inertia of fuel. The cases with higher vorticity strength and lower inertia of fuel (cases A, B1, and B2) show a faster increase of penetration distance. In the region between $x = 5$ and 10, however, the case with the lower inertia of fuel and lower injection pressure (case B2) shows a more rapid decrease of the slope of penetration distance because it experiences stronger deceleration of the upward flow of the fuel due to the high-pressure region over the fuel. Finally, case B2, with the most rapid decrease of penetration distance at the near field (with the highest pressure region under the fuel due to the strongest deceleration), shows the highest slope of penetration distance after $x = 10$.

Figure 9 shows the comparison of mixing rates on a log-log scale. Mixing rate is defined as the decay rate of the maximum mass fraction of fuel. The trend of the mixing rate is similar to the experimental result of Waitz et al.[13,14] In all cases, there is an acceleration of mixing rate at the near field (convection-dominated regime), whereas there is linear decay of maximum mass fraction of fuel at the far field (diffusion-dominated regime). Among the cases with the same fuel density (cases A, B1, and B2), cases B1 and B2 with lower injection pressure show the higher mixing rates. This is due to: 1) the jets for cases B1 and B2 are smaller than those for case A (see Fig. 6) and 2) the jets for cases B1 and B2 have axial velocities 8 ~ 9% lower than the freestream velocity, which can lead to improved mixing (see Tables 2 and 3). Among the cases with the same injection pressure (cases A, C1, and C2), cases C1 and C2, with higher density ratio (lower density gradient), show the lower mixing rate due to weaker baroclinic torque.

Figure 10 shows the mass flux of unburned hydrogen normalized by the mass flux initially injected. The relative burning rate is expressed in terms of the reduction rate of the hydrogen mass flux. For all cases, there are accelerations of burning rate at the near field, whereas the burning rates become constant at the far field (after about $x = 12$). This is believed to be the change of the mixing regime from the convection-dominated regime to the diffusion-dominated regime. In general, cases C1 and C2, with higher density ratio, i.e., the lower density gradient, result in the lower relative burning rate.

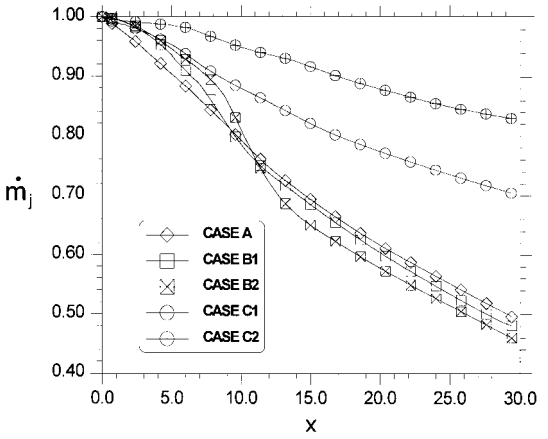

Fig. 10 Comparison of relative burning rate estimated by decay rate of hydrogen mass flux normalized by its own injection mass flux.

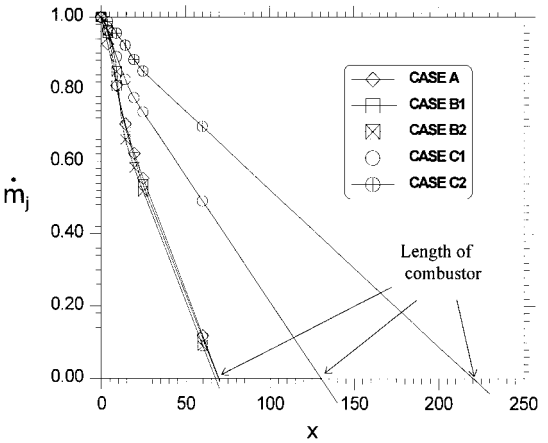

Fig. 11 Estimations of minimum combustor length required for complete combustion; the latter part after $x = 30$ is obtained with linear extrapolation.

Although it would be expected that the case with a higher fuel temperature has a higher burning rate, there exist regions where the case with a lower fuel temperature shows a higher burning rate. Case A, B1, and B2 with the same fuel density have different fuel temperatures. Although case A with the highest fuel temperature ($T_j = 1000$ K) has the fastest fuel consumption at the near field, case B2 with lowest fuel temperature ($T_j = 250$ K) has a sharp increase of fuel consumption after about $x = 8$, i.e., the trend of fuel consumption rate is reversed. This is due to the difference of time required for heating the fuel to a combustible state. Case B2 has the highest mixing rate, whereas it requires the longest time to heat the fuel to a combustible state because of its lowest temperature. Therefore, case B2 has the lowest burning rate during the heating period, but it has the highest burning rate after the heating period.

Figure 11 shows the prediction of the minimum combustor length required for complete combustion. These results are estimated by the linear extension of the results in Fig. 10 with the assumption that the burning rate at the far field (diffusion-dominated regime) is constant. The minimum combustor length required for complete combustion is the distance at which the mass flow of unburned fuel is reduced to zero. The combustor lengths for cases A, B1, and B2 are almost the same value of about 70 in. (1.8 m) and are about 130 in. (3.3 m) for case C1 and about 220 in. (5.6 m) for case C2. It is found that the combustor length required for complete combustion is dependent on the density (mass flow rate) of hydrogen, whereas other properties such as fuel temperature and pressure have little effect on the combustor length.

Conclusions

A computational investigation of the combustion process with shock-enhanced mixing is presented with Marble's combustor model of a scramjet engine using the three-dimensional Navier–Stoke equations and the k–ω turbulence model. The parameters such as circulation, penetration distance, mixing rate, and burning rate are introduced to investigate the mixing and combustion in a supersonic airstream. Using these parameters, the effects of the fuel conditions, such as pressure, density, and temperature, on combustion are investigated. The conclusions from computational results are as follows.

There is little difference between reacting and nonreacting cases in the mixing characteristics such as circulation, penetration distance, and mixing rate. This is believed to be because chemical reaction, i.e., heat release, has little influence on the generation of vorticity, which is the same trend found in Ref. 11. These results suggest that the mixing process strongly affects the combustion process and is not significantly affected by the combustion process in the shock-enhanced mixing. Therefore, the combustion process in a hypersonic flowfield can be decoupled from the mixing process with a only small differences in the trends.

The mixing regimes are of two distinct types: a convection-dominated regime and a diffusion-dominated regime. The convection-dominated regime is found at the near field of the fuel nozzle, where the shock-induced vorticity is generated. Hence, there are large changes in circulation, mixing rate, penetration distance, and burning rate. The diffusion-dominated regime is found at the far field, where there are no significant flow acceleration mechanisms; there are only small changes in circulation, penetration rate, mixing rate, and burning rate.

Two types of parametric studies were conducted. It is shown that changing the fuel temperature with the fuel density held fixed makes little difference in the mixing and combustion processes. The variation of the fuel density with the fuel pressure held fixed, on the other hand, makes significant differences in mixing rate and burning rate: The cases with lower density ratios have higher circulation, higher mixing rates, and higher relative burning rates. The case with higher density ratio, i.e., the lower density gradient, produces lower mixing rate and lower burning rate. This indicates that the mixing process is strongly influenced by the shock-induced vorticity because the strength of vorticity is determined by the interaction of the shock and the density gradient between the fuel and air. Also, at the near field, it is found that the strong vorticity is produced by the interaction between the shock and the density gradient and that the entrained hot air results in autoignition in all cases of our study, even when the temperature of the fuel is very low (for example, 250 K in cases B2 and C2). This indicates that the fuel temperature is not an important factor for the ignition process if the air temperature is high enough.

Finally, it is found that the parameter determining the combustor length required for complete combustion is the density, i.e., flow rate, of the fuel, whereas other properties such as fuel temperature and pressure have little effect on the combustor length. The combustor length is estimated by a linear extension of the fuel consumption graph with the assumption that the burning rate at the far field (diffusion-dominated regime) is constant.

Acknowledgments

The authors would like to acknowledge the Korea Science and Engineering Foundation for supporting this research under Contract 961-1005-043-2. The authors highly appreciate the thoroughness of the reviewers' comments.

References

[1] Billig, F. S., "Research on Supersonic Combustion," *Journal of Propulsion and Power*, Vol. 9, No. 4, 1993, pp. 499–514.

[2] Bogdanoff, D. W., "Advanced Injection and Mixing Techniques for Scramjet Combustors," *Journal of Propulsion and Power*, Vol. 10, No. 2, 1994, pp. 183–190.

[3] Bushnell, D. M., "Hypervelocity Scramjet Mixing Enhancement," *Journal of Propulsion and Power*, Vol. 11, No. 5, 1995, pp. 1088–1090.

[4] Rudinger, G., and Somers, L. M., "Behaviour of Small Regions of Different Gases Carried in Accelerated Gas Flows," *Journal of Fluid Mechanics*, Vol. 7, 1960, pp. 161–176.

[5] Haas, J. F., and Sturtevant, B., "Interaction of Weak Shock Waves with Cylindrical and Spherical Gas Inhomogeneities," *Journal of Fluid Mechanics*, Vol. 181, 1988, pp. 41–76.

[6] Marble, F. E., Hendricks, G. J., and Zukoski, E. E., "Progress Toward Shock Enhancement of Supersonic Combustion Processes," AIAA Paper 87-1880, July 1987.

[7]Jacobs, J. W., "Shock Induced Mixing of a Light Gas Cylinder," *Journal of Fluid Mechanics*, Vol. 234, 1992, pp. 629–649.

[8]Picone, J. M., and Boris, J. P., "Vorticity Generation by Shock Propagation Through Bubbles in a Gas," *Journal of Fluid Mechanics*, Vol. 189, 1988, pp. 23–51.

[9]Yang, J., Kubota, T., and Zukoski, E. E., "An Analytical and Computational Investigation of Shock-Induced Vortical Flows," AIAA Paper 92-0316, Jan. 1992.

[10]Drummond, J. P., "Mixing Enhancement of Reacting Parallel Fuel Jets in a Supersonic Combustor," AIAA Paper 91-1914, July 1991.

[11]Ton, V. T., Karagozian, A. R., Marble, F. E., Osher, S. J., and Engquist, B. E., "Numerical Simulations of High-Speed Chemically Reacting Flow," *Theoretical and Computational Fluid Dynamics*, Vol. 6, 1994, pp. 161–179.

[12]Marble, F. E., Zukoski, E. E., Jacobs, J. W., Hendricks, G. J., and Waitz, I. A., "Shock Enhancement and Control of Hypersonic Mixing and Combustion," AIAA Paper 90-1981, July 1990.

[13]Waitz, I. A., Marble, F. E., and Zukoski, E. E., "A Systematic Experimental and Computational Investigation of a Class of Contoured Wall Fuel Injectors," AIAA Paper 92-0625, Jan. 1992.

[14]Waitz, I. A., Marble, F. E., and Zukoski, E. E., "Investigation of a Contoured Wall Injector for Hypervelocity Mixing Augmentation," *AIAA Journal*, Vol. 31, No. 6, 1993, pp. 1014–1021.

[15]Lee, S. H., Jeung, I.-S., and Lee, S., "Application of Shock-Enhanced Mixing to Circular Cross-Sectional Combustor," AIAA Paper 96-0730, Jan. 1996.

[16]Marble, F. E., "Hottel Plenary Lecture: Gasdynamic Enhancement of Non-Premixed Combustion," *Twenty-Fifth Symposium (International) on Combustion*, Combustion Inst., Pittsburgh, PA, 1994, pp. 1–12.

[17]Hirsch, C., *Numerical Computation of Internal and External Flows*, Wiley, New York, 1990, pp. 408–594.

[18]Anderson, D. A., Tannehill, J. C., and Pletcher, R. H., *Computational Fluid Mechanics and Heat Transfer*, Hemisphere, Washington, DC, 1984, pp. 417–518.

[19]Hoffmann, K. A., *Computational Fluid Dynamics for Engineers*, Engineering Education System, Austin, TX, 1989, pp. 306–369.

[20]Reid, C. R., Prausnitz, J. M., and Poling, B. E., *The Properties of Gases and Liquids*, 4th ed., McGraw–Hill, New York, 1988, pp. 388–631.

[21]Gardiner, W. C., Jr., *Combustion Chemistry*, Springer–Verlag, New York, 1984, pp. 485–504.

[22]Evans, J. S., and Schexnayder, C. J., "Influence of Chemical Kinetics and Unmixedness on Burning in Supersonic Hydrogen Flames," *AIAA Journal*, Vol. 18, No. 2, 1980, pp. 188–193.

[23]Rogers, R. C., and Chinitz, W., "Using a Global Hydrogen-Air Combustion Model in Turbulent Reacting Flow Calculations," *AIAA Journal*, Vol. 21, No. 4, 1983, pp. 586–593.

[24]Wilcox, D. C., *Turbulence Modeling for CFD*, DCW Industries, La Cañada, CA, 1993, pp. 73–212.

[25]Patel, V. C., Rodi, W., and Scheuerer, G., "Turbulence Models for Near-Wall and Low Reynolds Number Flows: A Review," *AIAA Journal*, Vol. 23, No. 9, 1985, pp. 1308–1319.

[26]Yungster, S., "Numerical Study on Shock-Wave/Boundary Layer Interactions in Premixed Combustible Gases," *AIAA Journal*, Vol. 30, No. 10, 1992, pp. 2379–2387.

[27]Roe, P. L., "Approximate Riemann Solvers, Parameter Vectors, and Difference Schemes," *Journal of Computational Physics*, Vol. 43, No. 3, 1981, pp. 352–372.

[28]Anderson, W. K., and Thomas, J. L., "Comparison of Finite Volume Flux Vector Splitting for the Euler Equations," *AIAA Journal*, Vol. 24, No. 9, 1986, pp. 1453–1460.

[29]Yoon, S., and Jameson, A., "Lower–Upper Symmetric-Gauss–Seidel Method for the Euler and Navier–Stokes Equation," *AIAA Journal*, Vol. 26, No. 9, 1988, pp. 1025, 1026.

[30]Shuen, J. S., and Yoon, S., "Numerical Study of Chemically Reacting Flows Using a Lower–Upper Symmetric Successive Overrelaxation Scheme," *AIAA Journal*, Vol. 27, No. 12, 1989, pp. 1752–1760.

K. Kailasanath
Associate Editor